Hindawi Publishing Corporation
EURASIP Journal on Advances in Signal Processing
Volume 2010, Article ID 454705, 7 pages
doi:10.1155/2010/454705

Research Article

Use of the Location Inverse Solution to Reduce Ghost Images

Yong-Zhong Hu, Ting-Jun Li, and Zheng-Ou Zhou

School of Electronic Engineering, University of Electronic Science and Technology of China, Chengdu 610054, China

Correspondence should be addressed to Yong-Zhong Hu, huyz@uestc.edu.cn

Received 22 January 2009; Revised 31 July 2009; Accepted 7 October 2009

Academic Editor: Carlos Lopez-Martinez

Through-the-wall imaging (TWI) is a difficult but important task for both law enforcement and military missions. Acquiring information on both the internal features of a structure and the location of people inside plays an important role in many fields such as antiterrorism, hostage search and rescue, and barricade situations. Up to now, a number of promising experimental systems have been developed to validate and evaluate diverse imaging methods, most of which are based on a linear antenna array to obtain an image of the objects. However, these methods typically use the backward projection (BP) algorithm based on ellipse curves, which usually generates additional ghost images. In this paper, the algorithm using the location inverse solution (LIS) to reduce the ghost images is proposed and simulated. The results of simulation show that this approach is feasible.

1. Introduction

Imaging through obstacles such as walls, doors, and other visually opaque materials using microwave signals is considered a powerful tool for a variety of applications in both military missions and commercial enterprises. To achieve two-dimensional image reconstruction requires the resolution of scattered objects in both range and cross range directions.

In order to create an image of the interior of an obstacle, the probing signal must be able to pass through the obstacle with little attenuation. For through-the-wall imaging systems the material properties of the wall determine the degree to which a system can be successful. The major considerations are the absorption and refraction losses for the penetrating radiation. Data taken by Frazier [1] show that most building material is relatively transparent from 250 MHz to 3 GHz. So a system that uses frequencies below 3 GHz has the best chance of seeing through walls. Above 3 GHz, the attenuation in all materials begins to increase rapidly. This limits the range resolution but a 3 GHz bandwidth is wide enough to work successfully in many fields of application.

Resolution in the cross range direction is a function of the antenna aperture. One approach is to move the radar to acquire data at various intervals and then to synthesize an antenna aperture to obtain higher cross range resolution, but this method makes the operation and processing work more difficult and increases the cost of the system in practice. Another approach is to keep the radar at a fixed location and synthesize an aperture from a linear antenna array. This method is widely used, owing to its inherent advantages such as ease of operation and processing and so forth [2].

Hunt and his colleagues developed a through-the-wall imaging (TWI) system with a linear antenna array and simulated the approach of using a randomly spaced antenna array to decrease the ghost images. Using a randomly spaced antenna array to reduce ghost images will not always produce good results for all randomly spaced patterns, and, in practice, this structure has the added burden of excessive processing work [3]. This paper introduces the use of the location inverse solution (LIS) in the traditional BP imaging algorithm to partially reduce the ghost images

2. Ghost Image

The basic method of reconstructing an image of the inside of an obstacle consists of sampling the scattered signals and using backward projection (BP) algorithms to remove ambiguities in the location of objects, which scatter the probing signal. This forms an image of the inside of the

obstacle showing the relative locations of objects causing the signal scatter [4–6].

For a linear antenna array, data are collected by scanning one antenna pair of the array at a time. One antenna transmits while the other receives. For example, supposing a system with 4 antennas, we can get 12 independent combinations. Each individual transmit/receive antenna pair creates a range profile for all of the objects creating scatter in the antenna field of view. The bistatic range to each object in the image map is used as an index in the range profile. For a different antenna pair, the bistatic range to the same object will be different. The values from all of the antenna pairs from the scanning array are summed for each pixel in the image map. Where there are objects in the image that result in scattering, the individual observations from the antenna pairs will be in phase and sum to a large value. Where there are no objects, the individual observations will be out of phase and tend to sum towards zero. The magnitude of the summation depends on the radar cross section of the scattering object and the distance from the antenna array [3]. Figure 1 shows a schematic view of the reconstruction of a point object in the image map for a 4-element array.

Suppose that the transmitting pulse signal is $s(t)$, then the output of the nth receiver is given by

$$s_{nr}(t) = a_n s(t - \tau_n) + n(t), \tag{1}$$

where a_n is the attenuation coefficient, τ_n is the propagation delay associated with the object position and the parameters of the wall (namely, the wall thickness and its dielectric constant), and $n(t)$ is the noise signal. Suppose that there are m objects in the image field. Then, the output of the nth receiver is given by

$$s_{nr}(t) = \sum_{i=1}^{m} a_{ni} s(t - \tau_{ni}) + n(t), \tag{2}$$

where a_{ni} is the attenuation coefficient relevant to the ith object, and τ_{ni} is the propagation delay associated with the ith object position and the parameters of the wall. After sampling, the output of the nth receiver is given by

$$s_{nr}(k) = \sum_{i=1}^{m} a_{ni} s(k\Delta t - \tau_{ni}) + n(k\Delta t), \tag{3}$$

where Δt is sampling interval, and k is the sampling number, which is defined as $k \in [1, 2, \ldots, k_{\max}]$. Each $s_{nr}(k)$ is used to depict an ellipse curve to form the image of the objects. The ellipse curve or propagation delay contour curve is a standard ellipse curve if it ignores the presence of wall, but it is distorted to a quasiellipse curve if it takes into account the presence of the wall. Suppose that $I(x, y)$ is the imaging pixel matrix function, where (x, y) are the coordinates location of the pixel in the imaging field. Then, $I(x, y)$ is defined as follows:

$$I(x,y) = \begin{cases} \sum_{n=1}^{n_{\max}} \sum_{k=1}^{k_{\max}} s_{nr}(k), & \text{if } \tau_{s_{nr}(k)} = \tau_{n(x,y)}, \\ 0, & \text{if } \tau_{s_{nr}(k)} \neq \tau_{n(x,y)}, \end{cases} \tag{4}$$

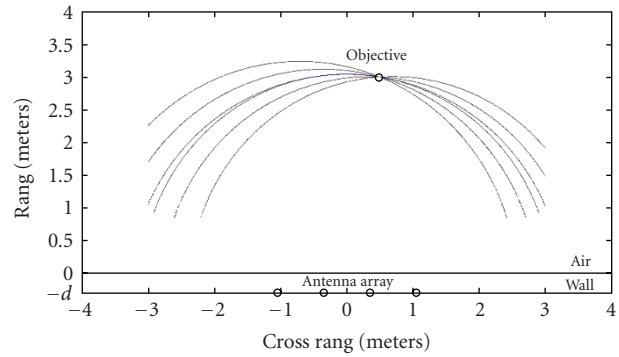

Figure 1: Reconstruction of a point object in the image map.

where $I(x, y)$ indicates the pixel intensity at location (x, y) of the imaging field, $\tau_{s_{nr}(k)}$ is the corresponding propagation delay of the sampling data $s_{nr}(k)$, and $\tau_n(x, y)$ is the corresponding propagation delay of the location (x, y) to the nth antenna pair.

Figure 2 is an original imaging result of six point objects, located at $(-0.5, 2), (0, 2), (0.5, 2), (-0.5, 3), (0, 3)$, and $(0.5, 3)$, the wall thickness is $d = 0.3$ m, and the wall dielectric constant is $\varepsilon_r = 9$.

Generally, the location of an object in the imaging field always has a large value due to the sum of in phase components (as shown in Figure 1). If there are more than one point object needed to be imaged with the ellipse curve set, some ghost images will exist due to the intersections of the different ellipse curve sets. Some intersections also have a relatively large value due to the sum of the in-phase curves and then generate false objects in the imaging field. Figure 3 shows a schematic view of the generation of a ghost image due to the intersections of the different ellipse curve sets.

Theoretically, an increase in the number of antennas and objects needed to be imaged will generate more intersections, which consequently generate more ghost images in the image field.

3. Algorithm Simulation and Analysis

In order to simulate the imaging algorithm, an imaging system is assumed as shown in Figure 4, in which a linear antenna array is placed against the wall with four of the same antennas each spaced 0.7 m apart from its neighbor. The wall material is uniform with a thickness d and a dielectric constant ε_r. The system emits 0.4 nanosecond-width pulse signals to probe the image field. The bandwidth is 2.5 GHz and the six assumed point objects are located at $(-0.5, 2), (0, 2), (0.5, 2), (-0.5, 3), (0, 3)$, and $(0.5, 3)$. Suppose that the noise function $n(t)$ is a normal random function, the sampling interval is $\Delta t = 0.07$ ns, the sampling number is enough to image the view field, and the three point objects close to the antenna array have a three times greater scattering intensity than the other three point objects. In order to simplify the simulation, we suppose that the 12 propagation delay contour curves corresponding to 12 antenna pair combinations have the same intensity for

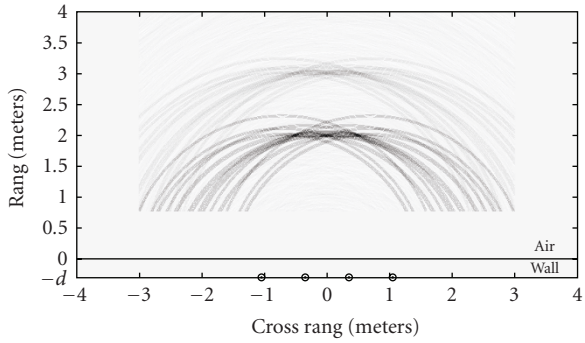

(a) 2-D image

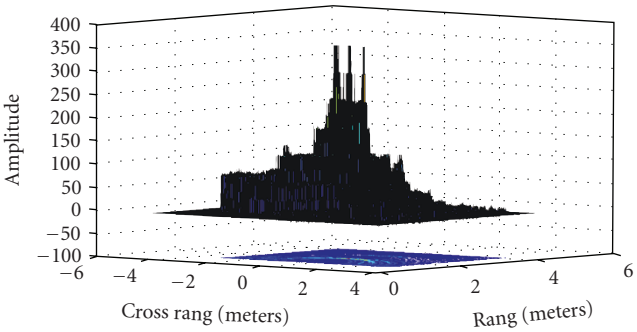

(b) 3-D view of data

Figure 2: An original imaging result of six point objects, $d = 0.3$ m, $\varepsilon_r = 9$.

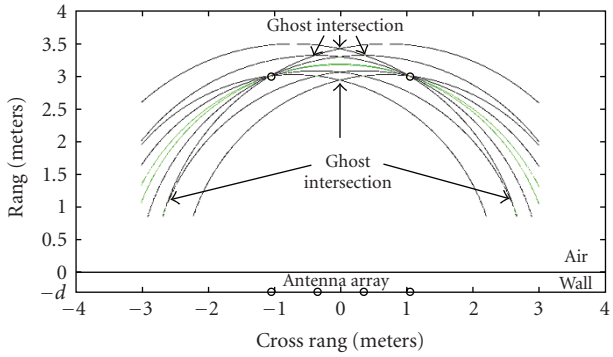

Figure 3: An illustration of the ghost intersection.

each point object, although, in practice, they are generally different due to the different traveling distances and the different scattering characteristics relevant to the different incident angles to the object.

As show in Figure 5, the propagation delay τ, incurred by the signal as it travels from the transmitter located at $(xt, -d)$, to the target located at $P(Xp, Yp)$, and back to the receiver located at $(xr, -d)$, is given by

$$\tau = \frac{r_1 + r_2}{v} + \frac{R_1 + R_2}{c}, \tag{5}$$

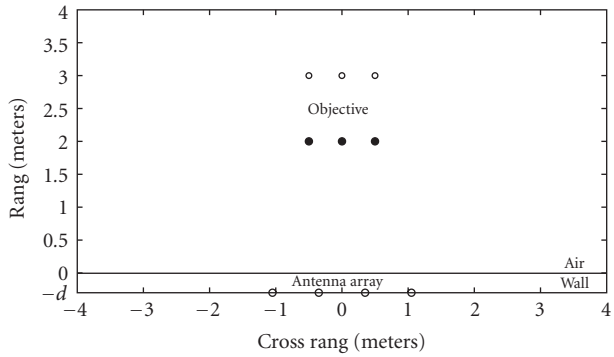

Figure 4: The scene of simulation.

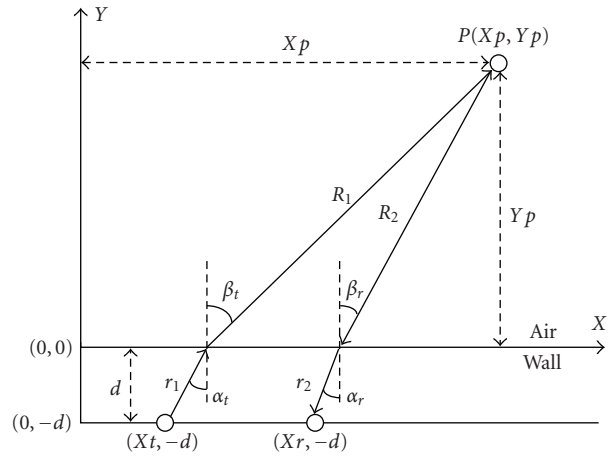

Figure 5: Geometry for computing propagation delay on reception.

where r_1 and r_2 are the traveling distance of signal in the wall, respectively, and R_1 and R_2 are the traveling distance of signal in the air, respectively. c is the speed of the signal traveling in the air, and v is the speed of the signal traveling in the wall material with a dielectric constant ε_r, and $v = c/(\sqrt{\varepsilon_r})$. For a signal, traveling from a wall material with a dielectric constant ε_r to the air and incident at an angle α, the angle of refraction β can be computed by Snell's law [7]:

$$\sin\beta = \sqrt{\varepsilon_r}\sin\alpha, \tag{6}$$

and the propagation delay contour depicted by the sampling data is distorted to a quasiellipse curve due to the propagation speed change and the refraction between the wall and the air.

In the following, we will discuss the imaging results for both known and unknown wall parameters.

3.1. Wall Parameters Are Known. In this section, we suppose that the wall parameters are known *a priori*. We assume that the wall dielectric constant is $\varepsilon_r = 9$ (corresponding to a concrete wall [1]), and the wall thickness is $d = 0.3$ m.

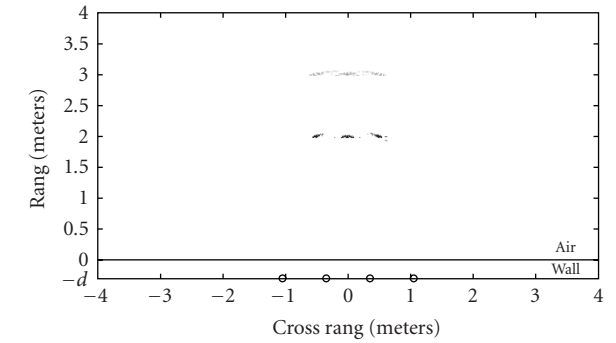

(a) 2-D image

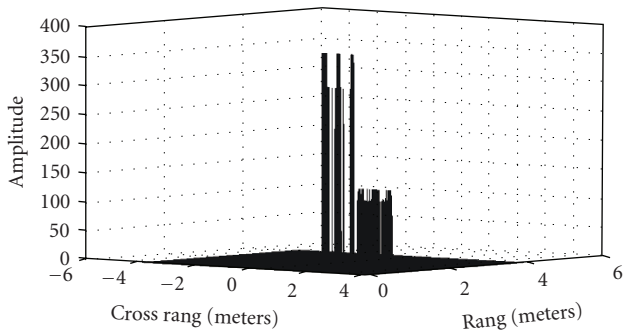

(b) 3-D view of data

Figure 6: Imaging result using IPF.

As shown in Figure 5, the propagation delay τ_p corresponding to the point object P can be computed by (5), where r_1, r_2, R_1, and R_2, can be computed by

$$r = \frac{d}{\cos\alpha}, \qquad R = \frac{y_p}{\cos\beta}, \tag{7}$$

and then we use (4)–(7) to generate the original imaging result as shown in Figure 2.

In Figure 2, besides the image of six point objects, there are a large number of ghost images. The intensities of some ghost images are even stronger than the intensities of the three weak point objects (i.e., the three point objects far away from the antenna array in Figure 4). To get the correct image of objects, ghost images need to be eliminated. Using an imaging probability function (IPF) to remove the ghost images is a feasible approach [8]. It comes from an initial assumption that if all the receivers receive the scattering signal, then the location of an object in the image field will have 12 addition operations in phase due to the 4 antennas, whereas the location, where has no object in the image field, will have relatively less probability of getting addition operations in phase. Therefore, the object can be distinguished from the ghost image by using proper imaging probability gating. Figure 6 shows the result of using an imaging probability function (IPF) to reduce ghost images. Compared with the original image (as shown in Figure 2), the imaging quality of Figure 6 has been significantly improved.

Although the imaging result of Figure 6 is gratifying, several ghost images distributed in the image field can still be found. These ghost images result in the presence of false objects and prevent the images of the objects from being focused on their centers. This is mainly due to the inherent disadvantage of the imaging algorithm using ellipse curves. To further suppress the ghost image, we introduce the approach of using the location inverse solution.

Firstly, suppose that (xi, yi) is the coordinate location of the ith object in the image field, and the $(xj, -d)$ is the coordinate location of the jth antenna. When the $j1$th antenna transmits pulse signals, and the $j2$th antenna receives signals scattered by the ith object, the corresponding propagation delay can be computed by

$$\tau_{il} = \frac{r_{1\_j1} + r_{2\_j2}}{v} + \frac{R_{1\_j1} + R_{2\_j2}}{c}, \tag{8}$$

where the τ_{il} is the propagation delay from the $j1$th antenna to the ith object and scattered to the $j2$th antenna, l is the number of antenna pair, and $l \in [1, 2, \ldots, 12]$. Then the corresponding location of the ith object in the sampling data of the lth antenna pair can be computed by

$$k_{il} = \text{round}\left(\frac{\tau_{il}}{\Delta t}\right) \tag{9}$$

using (8) and (9), and the locations of the ith object in the 12 antenna pairs can be computed as $\{k_{i1}, k_{i2}, \ldots, k_{i12}\}$.

Secondly, we use the sampling data corresponding to the 12 locations within the 12 sampling channels to recalculate the pixel intensity at the location (xi, yi) of the imaging field, as follows:

$$I(x_i, y_i) = \sum_{l=1}^{12} s_{lr}(k_{il}) \tag{10}$$

and then recalculate the imaging probability function $P(xi, yi)$ as follows:

$$p(x_i, y_i) = \begin{cases} p(x_i, y_i) + \dfrac{1}{12}, & \text{if } \Delta I(x_i, y_i) > 0, \\ p(x_i, y_i) - \dfrac{1}{12}, & \text{if } \Delta I(x_i, y_i) < 0. \end{cases} \tag{11}$$

$|p(xi, yi)|$ indicates the probability of the summation operation being in phase. If the ith object is a false object, its $|p(xi, yi)|$ will obviously be less than 1. Therefore, we can easily distinguish the true object from the ghost image by using a proper gating of the imaging probability function.

The same procedure is repeated for all the other objects in the image field. Figure 7 is the imaging result by using the location inverse solution approach. Compared with Figures 6 and 7 shows that the ghost images have been reduced even more, and the centers of the images of point objects have been better focused.

3.2. Wall Parameters Are Unknown. In a practical situation, the values of the wall parameters usually are not exactly known. Although some researchers have proposed various approaches for estimating the material parameters of an

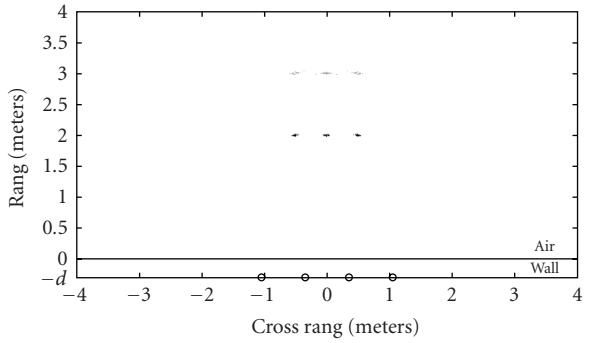

(a) 2-D image

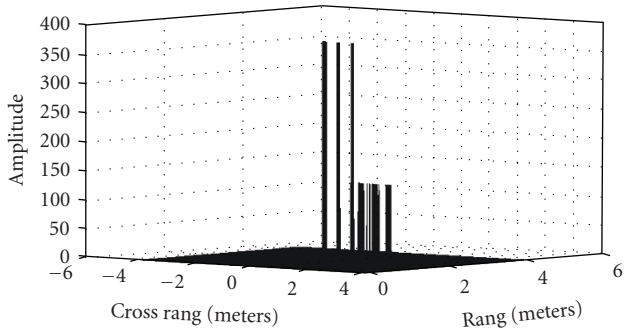

(b) 3-D view of data

Figure 7: Imaging result using LIS, while $d_e = d_t = 0.3\,\text{m}$, and $\varepsilon_{re} = \varepsilon_{rt} = 9$.

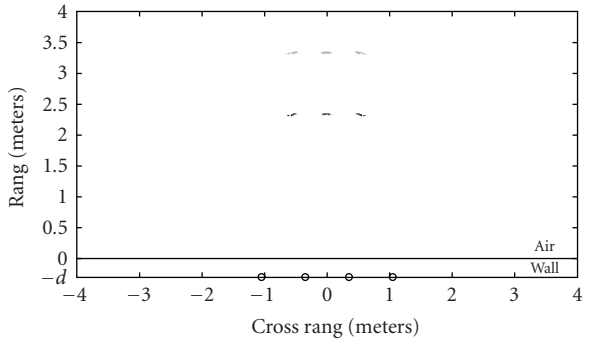

(a) 2-D image

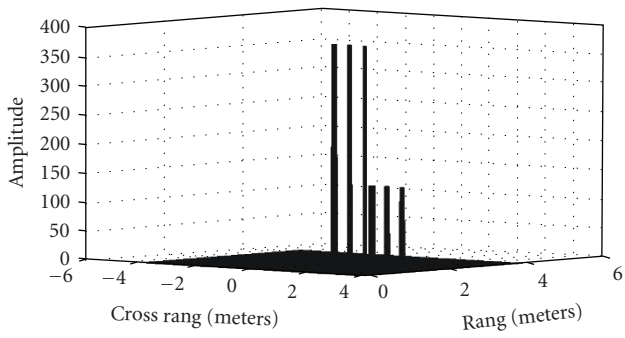

(b) 3-D view of data

Figure 8: Imaging result using LIS, while $d_e = 0.2\,\text{m}, d_t = 0.3\,\text{m}$, and $\varepsilon_{re} = \varepsilon_{rt} = 9$.

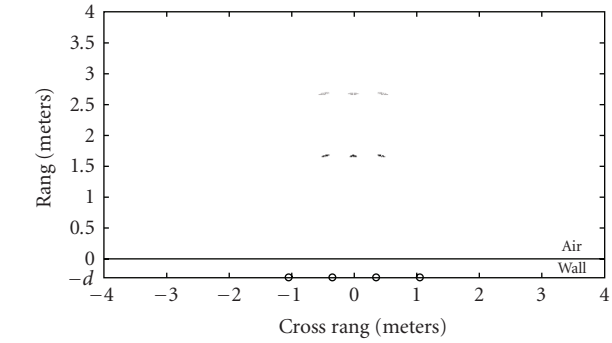

(a) 2-D image

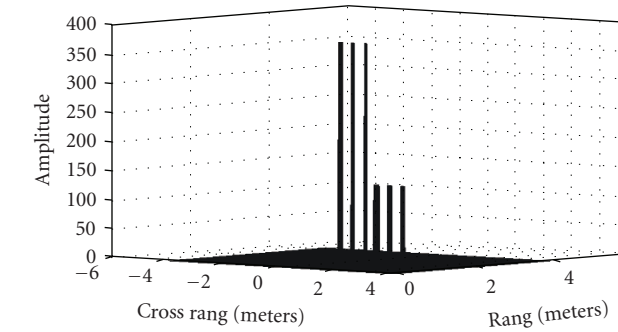

(b) 3-D view of data

Figure 9: Imaging result using LIS, while $d_e = 0.4\,\text{m}$, $d_t = 0.3\,\text{m}$, and $\varepsilon_{re} = \varepsilon_{rt} = 9$.

unknown wall on site [7], to get the exact parameters of the unknown wall in real time is still difficult. It is usual to estimate values from the literature and employ experience in substituting these for the true values of the wall parameters in practice. To demonstrate the simulation experiment, we specify that d_e is the estimated wall thickness, d_t is the true wall thickness, ε_{re} is the estimated wall dielectric constant, and ε_{rt} is the true wall dielectric constant.

Firstly, we analyze the effect of the wall thickness including error while the wall dielectric constant is known exactly, that is, $d_e = d_t + \Delta d, \varepsilon_{re} = \varepsilon_{rt} = 9$, where Δd is the error between the estimated thickness and the true thickness.

Figure 8 is the imaging result using location inverse solution to remove ghost images, while the estimated wall thickness is less than the true value, that is, $\Delta d < 0$. As shown in Figure 8, when $d_e < d_t$, the imaging locations of point objects are shifted far away from the antenna array.

Figure 9 is the imaging result using the location inverse solution to remove the ghost images, while the estimated wall thickness is larger than the true value, that is, $\Delta d > 0$. As shown in Figure 9, when $d_e > d_t$, the imaging locations of point objects are shifted close to the antenna array.

Secondly, we analyze the effect of the wall dielectric constant including error while the wall thickness is known exactly, that is, $d_e = d_t = 0.3\,\text{m}$, $\varepsilon_{re} = \varepsilon_{rt} + \Delta\varepsilon_r$, where $\Delta\varepsilon_r$ is the error between the estimated dielectric constant and the true dielectric constant.

Figure 10 is the imaging result using the location inverse solution to remove the ghost images, while the estimated wall

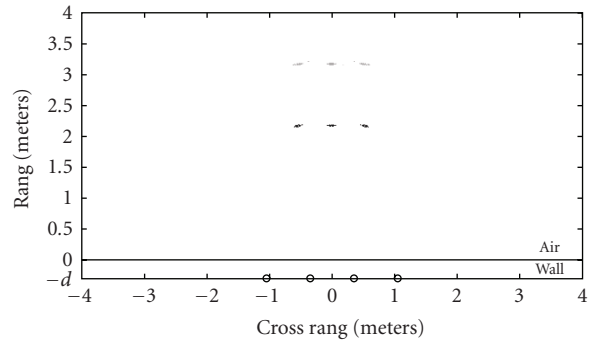

(a) 2-D image

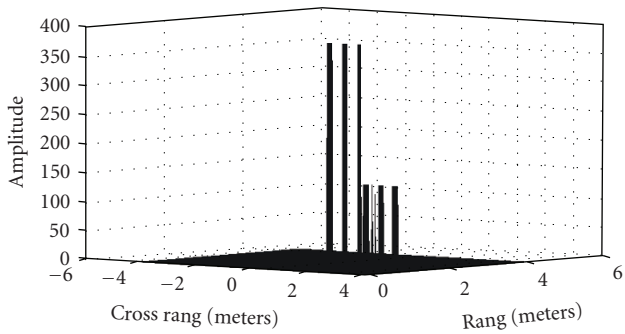

(b) 3-D view of data

Figure 10: Imaging result using LIS, while $d_e = d_t = 0.3$ m, and $\varepsilon_{re} = 6.25, \varepsilon_{rt} = 9$.

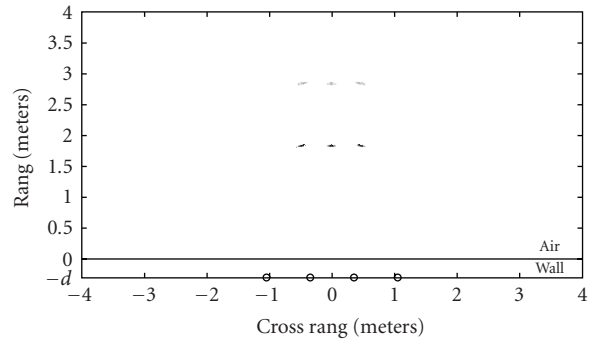

(a) 2-D image

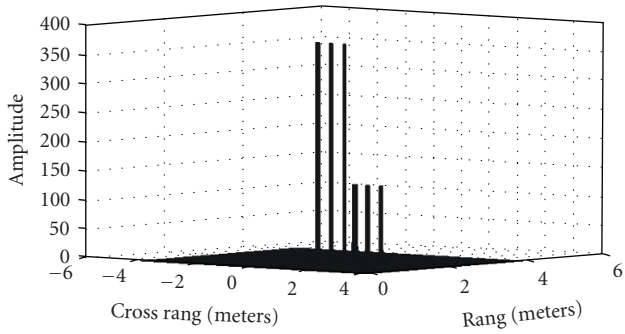

(b) 3-D view of data

Figure 11: Imaging result using LIS, while $d_e = d_t = 0.3$ m, and $\varepsilon_{re} = 12.25$, $\varepsilon_{rt} = 9$.

dielectric constant is less than the true value, that is, $\Delta\varepsilon_r < 0$. As shown in Figure 10, when $\varepsilon_{re} < \varepsilon_{rt}$, the imaging locations of point objects are shifted far away from the antenna array.

Figure 11 is the imaging result using the location inverse solution to remove ghost images, while the estimated dielectric constant is larger than the true value, that is, $\Delta\varepsilon_r > 0$. As shown in Figure 11, when $\varepsilon_{re} > \varepsilon_{rt}$, the imaging locations of point objects are shifted close to the antenna array.

In practice, when both of the wall parameters have errors, the final shift of the object's location will depend on the effects of both the wall thickness error and the wall dielectric constant error.

The simulation result of the object's location shift due to the errors of the wall parameters between the estimated value and the true value is consistent with the result of [7]. Figures 7–11 show that the approach, using the location inverse solution to remove the ghost image, is insensitive to the wall parameter ambiguities, and can work efficiently both when the wall parameters are known and unknown.

4. Conclusions

In this paper, a new algorithm using the location inverse solution based on IPF to reduce the ghost image is introduced. It can overcome the disadvantages of the conventional ellipse curve imaging algorithm. The results of simulation experiment show that it can effectively and significantly remove the ghost images whether the wall parameters are known or unknown. Furthermore, it will not deteriorate the imaging quality of weak scattering objects. Our results are based on simulations, and we are currently exploring real-time hardware implementation. In practice, proper preprocessing measures, such as antenna demodulation, noncoherent integration of multiple pulses, multichannel calibration and time delay compensation, and so forth, should be employed to enhance the quality of received signal [9, 10]. With current technological advances, such system can operate in near real-time thereby providing rapid and covert detection of target obscured by walls for antiterrorism and law enforcement applications.

Acknowledgment

This research was partly supported by the China Scholarship Council under Grant no. 2007A55018.

References

[1] L. M. Frazier, "MDR for law enforcement," *IEEE Potentials*, vol. 16, no. 5, pp. 23–26, 1997.

[2] F. Ahmad, G. J. Frazer, S. A. Kassam, and M. G. Amin, "Design and implementation of near-field, wideband synthetic aperture beam forms," *IEEE Transactions on Aerospace and Electronic Systems*, vol. 40, no. 1, pp. 206–220, 2004.

[3] A. R. Hunt, "Image formation through walls using a distributed radar sensor array," in *Proceedings of the 32nd Applied*

Imagery Pattern Recognition Workshop (AIPR '03), pp. 232–237, Washington, DC, USA, October 2003.

[4] W. Lei, C. Huang, and Y. Su, "A real-time BP imaging algorithm in SPR application," in *Proceedings of the IEEE International Geoscience and Remote Sensing Symposium (IGARSS '05)*, pp. 1734–1737, Seoul, Korea, 2005.

[5] W.-T. Lei, Y. Su, and C.-L. Huang, "Surface penetrating radar recursive back projection imaging algorithm," *Acta Electronica Sinica*, vol. 33, no. 12, pp. 2115–2119, 2005.

[6] Y. Zhao, C.-L. Huang, Y. Su, and L. Wentai, "BP imaging algorithm for UWB-TWDR," *Radar Science and Technology*, vol. 6, no. 1, pp. 49–54, 2007.

[7] G. Wang, M. G. Amin, and Y. Zhang, "New approach for target locations in the presence of wall ambiguities," *IEEE Transactions on Aerospace and Electronic Systems*, vol. 42, no. 1, pp. 301–315, 2006.

[8] Y.-Z. Hu, T. J. Li, and Z.-O. Zhou, "Use of imaging probability function to reduce ghost image," in *Proceedings of the International Conference on Apperceiving Computing and Intelligence Analysis (ICACIA '08)*, pp. 185–188, December 2008.

[9] R. Zetik, S. Crabbe, J. Krajnak, P. Peyerl, J. Sachs, and R. Thomä, "Detection and localization of persons behind obstacles using M-sequence through-the-wall radar," in *Proceedings of the Sensors, and Command, Control, Communications, and Intelligence (C3I) Technologies for Homeland Security and Homeland Defense V*, vol. 6201 of *Proceedings of SPIE*, pp. 1–12, 2006.

[10] E. J. Baranoski, "Through-wall imaging: historical perspective and future directions," *Journal of the Franklin Institute*, vol. 345, no. 6, pp. 556–569, 2008.